CRYSTAL GROWTH & DESIGN

Article

pubs.acs.org/crystal

In Situ Crystallization and Morphological Evolution in Multicomponent Indium Oxide Thin Films

Mahyar M. Moghadam,[†] Ran Li,[†] D. Bruce Buchholz, Qianqian Li, Peter W. Voorhees, and Vinayak P. Dravid*

Department of Materials Science and Engineering, Northwestern University, Evanston, Illinois 60208, United States

Supporting Information

ABSTRACT: The crystallization kinetics of $Zn_{0.3}In_{1.4}Sn_{0.3}O_3$ (ZITO-30) thin films is investigated via isothermal in situ transmission electron microscopy measurements. Extensive analysis is conducted to reveal the nucleation mechanism and growth rate at four different temperatures. The results show that the nucleation rate in this system is time-dependent and continuously decelerates following a power law decay. The crystal growth rate is constant at a given temperature, and interface-limited growth is the controlling mechanism in the kinetics of amorphous ZITO-30 crystallization. The activation energy for the overall process and interface growth are derived from the experimental data. A morphological study of the grains shows that the {100} interfaces have low mobility and are responsible for the anisotropic crystal shapes. It is found that the {111} and {100} planes of the crystal form parallel to the film−vapor interface during the nucleation process. The results demonstrate a rather complex yet tractable correlation between the experimental results and theoretical underpinning in complex multicomponent oxide thin films.

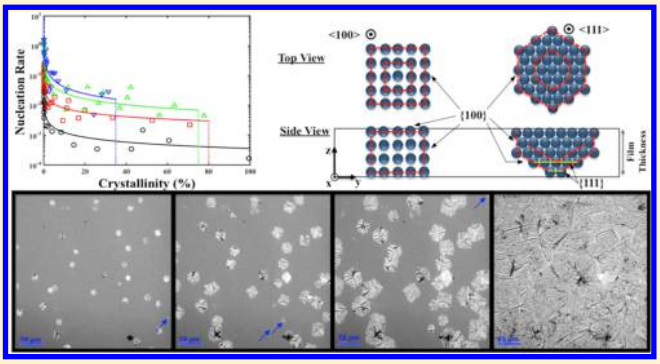

INTRODUCTION

Transparent conducting oxides (TCOs) exhibit both high electric conductivity and high optical transparency in the visible range. Since Badeker first reported that thin films of oxidized Cd could become both transparent and electrically conducting,[1] many other TCOs, like ZnO and In_2O_3, have been investigated to achieve better properties with lower cost. Because of the fast development of TCOs, they are now widely used in various technologies, including UV detectors,[2] fully transparent displays,[3] flexible electronics,[4] and energy-conversion devices and systems.[5] Compared to crystalline TCOs, amorphous (a-) TCOs can be deposited at a lower temperature, which enables them to be fabricated into thin-film transistors (TFTs) on temperature-sensitive plastic substrates.[6] Furthermore, a-TCOs can be integrated into flexible electronic devices with high conductivity, good interfacial properties, and high mechanical robustness without a postannealing process.[7−9]

Over the past decade in the TCO industry, Sn-doped In_2O_3 (ITO) has exhibited excellent performance in applications as a transparent electrode.[10] However, ITO also suffers from chemical instability,[11] a relatively low crystallization temperature of amorphous films,[12] inferior mechanical properties,[13] and mediocre surface uniformity.[14] Moreover, with the continuously increasing cost of indium, multicomponent-doped In_2O_3 materials have attracted the interest of many scientists because of their lower indium composition and favorable TCO properties that are almost the same as ITO.[15] Because Zn^{2+} has a vacant and spherically symmetrical $4s^0$ orbital, which could be overlapped by the s-orbitals in neighboring cations to control electrical conductivity,[14] researchers were able to successfully develop a new doped In_2O_3 system: Zn−In−Sn−O, so-called ZITO materials. While keeping the same bixbyite structure[16] as In_2O_3 and ITO, ZITO materials demonstrate a large decrease in indium content (as high as 70%[17,18]). In addition, ZITO materials also have good chemical stability, smooth surfaces, and, most importantly, high electrical conductivity (∼1400 S/cm).[17] Amorphous $Zn_{0.3}In_{1.4}Sn_{0.3}O_3$ (a-ZITO), in which 30% of the indium in the In_2O_3 structure is replaced by cosubstitution of zinc and tin (a-ZITO-30), performs the best among ZITO materials. Numerous studies of the defect structures,[19] surface properties,[20] and electrical and band gap properties[17] of a-ZITO-30 materials have been conducted, but few researchers have examined the thermodynamic process of a-ZITO-30. Previous X-ray diffraction and scanning transmission fluctuation electron microscopy (STFEM) studies indicated that a-ZITO-30 thin films grown by pulsed laser deposition (PLD) at different deposition temperatures have different structures with short-, medium-, and long-range ordering.[21,22] In situ wide-angle X-ray scattering (in situ GIWAXS) experiments[23] have also been conducted to explore the thermal stability of ZITO-30 thin films. These macroscopic studies investigated the crystallization

Received: December 16, 2016
Revised: January 25, 2017
Published: January 30, 2017

DOI: 10.1021/acs.cgd.6b01849
Cryst. Growth Des. XXXX, XXX, XXX−XXX

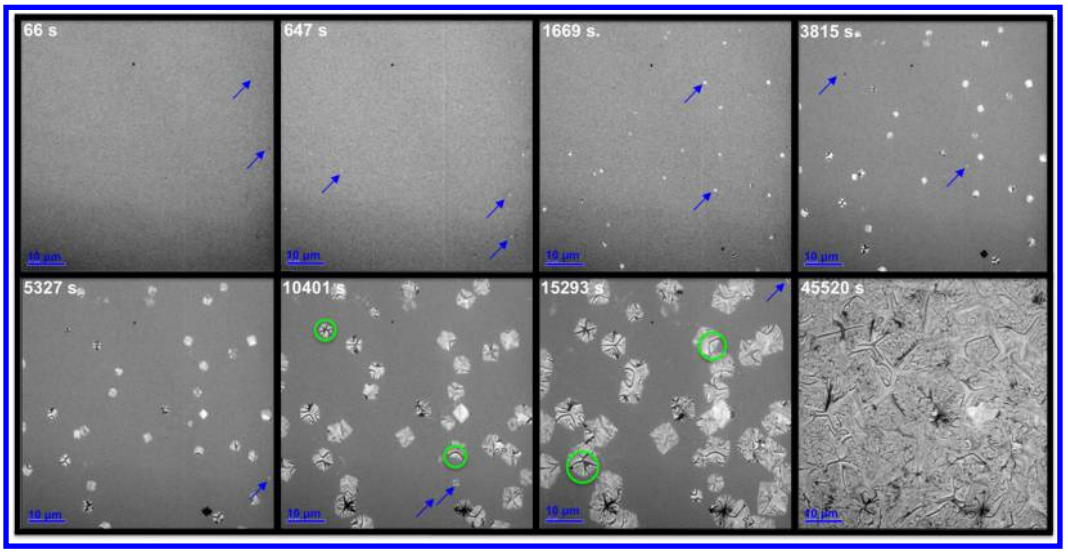

Figure 1. Bright-field TEM micrographs of ZITO-30 films crystallized to different extents. Arrows show new nuclei, which appear continuously during isothermal crystallization at 335 °C. Circles indicate some examples of bend contours.

temperature range and fit the in situ X-ray data into the Johnson–Mehl–Avrami–Kolmogorov (JMAK) equation. No nucleation mechanism or crystal growth geometry for a-ZITO-30 thin films has been reported. Having access to fundamental information like kinetics parameters is extremely important for processing and fabricating TCO materials like ZITO. These studies underscore the need to unravel the nucleation and growth processes of a-ZITO-30 thin films and to understand the role of the annealing temperature in this process.

Here, in situ TEM techniques are employed to investigate the kinetics of isothermal crystallization in $Zn_{0.3}In_{1.4}Sn_{0.3}O_3$ (a-ZITO-30) thin films. Four different temperatures are examined to determine kinetics parameters, including nucleation mechanism and growth rate. Activation energies for the overall process and interface growth are determined from the experiments. Furthermore, anisotropic behavior of crystallized grains is characterized for different grain morphologies and possible crystallographic orientations for grain growth and is discussed. Although these results are on nominal ZITO, the approach and findings should be applicable to many oxide systems containing such typical amorphous–crystalline phase transitions.

EXPERIMENTAL SECTION

Fabrication. ZITO30 thin films were grown by PLD from a dense hot-pressed zinc–indium–tin oxide ($Zn_{0.3}In_{1.4}Sn_{0.3}O_3$) target (25 mm diameter). PLD was accomplished with a 248 nm KrF excimer laser with a 25 ns pulse duration that was operated at 2 Hz. The 200 mJ/pulse beam was focused onto a 1 mm × 3 mm spot size. The target was rotated at 5 rpm about its axis to prevent localized heating. The target–substrate separation was fixed at 10 cm. The films were grown on NaCl crystalline substrates in an O_2 ambient of 7 mTorr with a deposition temperature of 100 °C. The film thickness was estimated to be ∼50 nm based on the calibrated deposition rate. The substrates were cleaved in air and attached to a resistively heated substrate holder with silver paint.

The NaCl substrates, on which the a-ZITO-30 thin films were grown, were detached from the a-ZITO-30 thin films by simple dissolution in deionized (DI) water. After nearly 2 min, the a-ZITO-30 thin films began floating on the surface of the DI water. TEM grids, 200 mesh copper with pure carbon supporting membrane, were used to lift out the thin films. The pure carbon membranes on the copper grid not only supported the thin films but also helped to conduct heat to the films from the hot stage in the heating holder.

Microscopy. The crystallinity of the postanneal films was observed with in situ heating TEM. The in situ heating TEM experiments were performed in a Hitachi 8100 TEM using a Gatan heating holder with a temperature range from room temperature to 900 °C. Previous in situ GIWAXS measurements showed that a-ZITO-30 thin films can remain amorphous under an annealing temperature of 300 °C.[23] Therefore, in the heating process, the temperature was directly set to 300 °C and allowed to stabilize at that temperature for 10 min. The temperature was then increased further to the desired annealing temperature, at which point the capture of images of the amorphous-to-crystalline process began. Videos were made from a series of images captured at the corresponding temperatures. The time and size information for each image was stored on a local computer disk.

High-resolution TEM (HR-TEM) images were taken with a GIF camera on a JEOL 2100F TEM at an accelerating voltage of 200 kV with thin films annealed halfway on TEM grids with carbon membrane support films. Corresponding diffraction patterns were taken with the upper camera on a JEOL 2100F TEM. Image processing and area measurement were carried out by Fiji (open source software) for image analysis.[24]

Characterization. Electron energy loss spectroscopy (EELS) spectra were obtained on a JEOL 2100F TEM operated in scanning transmission electron microscopy (STEM) mode with an aperture size of 5 nm and 0.3 eV/pixel dispersion. The EELS spectra of the four postannealed films show that their thicknesses are almost the same (see the Supporting Information).

Energy dispersive X-ray spectroscopy (EDX) mapping was conducted on a Hitachi HD-2300 scanning transmission electron microscope equipped with dual EDX detectors (Thermo Scientific NSS 2.3) with a 200 kV acceleration voltage. The specimens used were the same as those used for HR-TEM. Experimental conditions were set to 1001 frames with a pixel size of 3.24 nm^2 and a pixel dwell time of 50 μs.

STEM images of postannealed thin films were taken on a Hitachi SU8030 scanning electron microscope operated in STEM mode with an accelerating voltage of 30 kV.

RESULTS AND DISCUSSION

In situ isothermal crystallization experiments were conducted at 335, 355, 375, and 395 °C under 300× magnification. This provides sufficient area to observe a large number of nuclei (50–80) before complete crystallization occurs in order to determine the nucleation mechanism and growth rate. Then,

DOI: 10.1021/acs.cgd.6b01849
Cryst. Growth Des. XXXX, XXX, XXX–XXX

the experiments were repeated at higher magnification (1000×) to obtain better resolution of each grain in order to characterize the anisotropic behavior of the interface mobility.

Figure 1 shows different stages of the crystallization process via nucleation and growth under isothermal conditions. Due to the strain generated by the density difference between the amorphous domain and crystalline phase, the large crystals tend to bend, which results in a typical contrast feature known as bend contours,[25,26] as shown in Figure 1.

Figure 2 shows the temporal evolution of the fraction of crystalline area during crystallization. As expected, at higher

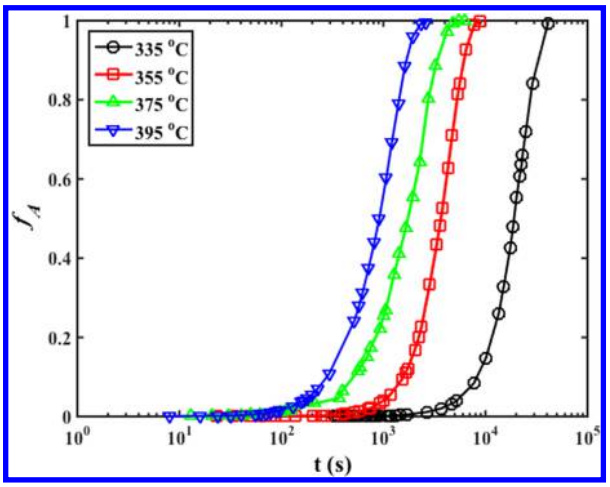

Figure 2. Temporal evolution of the fraction of crystalline area at different temperatures.

temperatures the system undergoes faster transformation. In particular, 50% crystallization at 395 °C is reached nearly 20 times faster than that at 335 °C. However, the average grain size at the end of transformation and incubation time (t_0) follows the opposite trend and decreases as the temperature increases (Figure 3a). In general, smaller average grain sizes can be explained by the presence of a larger number of nuclei inside the system, which is consistent with the nucleation rate being faster at higher temperature. The average grain size at the end of crystallization for the given temperature range varies from 9 to 11 μm. In this analysis, the average grain size is calculated based on a circularly equivalent area ($\bar{d} = 2\sqrt{\bar{A}/\pi}$), where $\bar{A}$ is the average grain area. The late stage limit, where the grain size is considerably larger than the film thickness, indicates that the crystallization occurs in 2D.[27,28]

The decrease in the incubation time as the temperature increases also has a classic explanation based on how fast the system can accumulate enough energy to overcome the activation barrier for crystallization. Following classic phase transformation theory, one can determine the overall activation energy of the crystallization process by calculating the slope of a $\ln[t_0]$ vs $1/k_BT$ plot. Conventionally, t_0 is defined as the time required for the first crystal to nucleate and grow large enough to be observable under the microscope, which obviously depends on the magnification applied. However, Edelman et al.[29] showed that the time to reach a fixed degree of crystallinity has the same exponential dependence as t_0 and only causes a shift in the Arrhenius plot. Thus, as shown in Figure 3b, t_0, $t_{5\%}$, $t_{10\%}$, and $t_{20\%}$ are used to determine the activation energy associated with the overall crystallization of a-ZITO-30. The

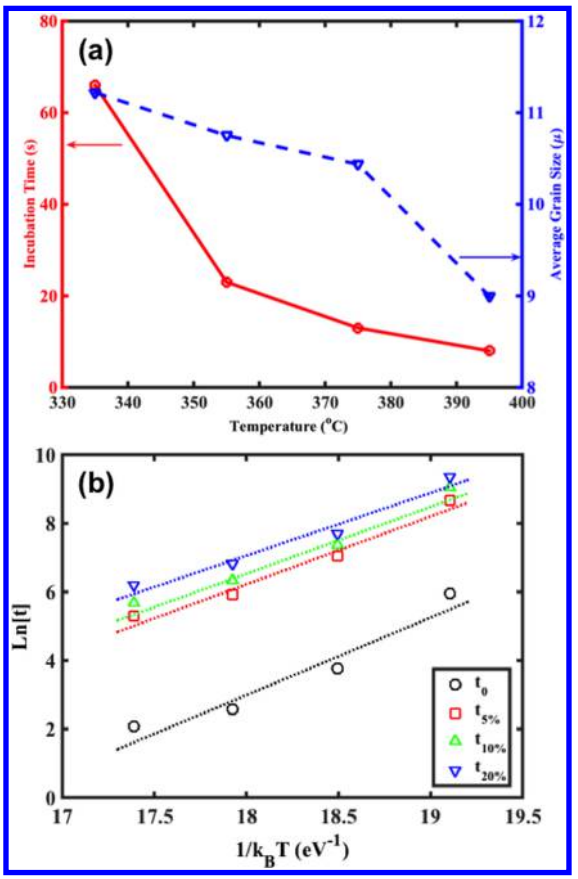

Figure 3. (a) Average grain size and incubation time at different temperatures. (b) Arrhenius plot to determine the temperature dependence of the incubation time for t_0, $t_{5\%}$, $t_{10\%}$, and $t_{20\%}$ crystallinity.

activation energy is found to be 2.0 ± 0.2 eV, which includes both nucleation and growth phenomena.

Nucleation. The majority of available methods to analyze crystallization kinetics assume time-independent nucleation either in the form of site-saturated nucleation or a constant nucleation rate.[27,30] Therefore, identification of the nucleation mechanism is the first step in a crystallization kinetics study. In situ isothermal experiments provide the opportunity to determine the nucleation rate ($\dot{N}$) by monitoring the number of new nuclei (N) and area fraction (f_A) of the crystalline phase over time as[31]

$$\dot{N}(t) = \frac{1}{[1 - f_A(t)]}\left(\frac{N_{t+\Delta t} - N_t}{\Delta t}\right) \quad (1)$$

Figure 4a, shows the nucleation rate for different temperatures. It is evident that the nucleation rate does not reach a constant during the time of crystallization for any of these temperatures. The linear trend in the log−log plot indicates that the nucleation rate follows power law decay ($\dot{N}(t) = 20t^{-1.1}$) as crystallization progresses, which means that, despite continued nucleation throughout the transformation, the rate keeps decelerating. The presence of power law decay also reveals an interesting point regarding the structural relaxation of a-ZITO-30 at a given temperature. Classic nucleation theory gives the nucleation rate as $\dot{N} = N_0 \exp(-W/k_BT)$, where N_0 is associated with the number of nucleation sites and W is the energy barrier of the nucleation, which involves two terms, one associated with the changes in the bulk free energy and the

DOI: 10.1021/acs.cgd.6b01849
Cryst. Growth Des. XXXX, XXX, XXX−XXX

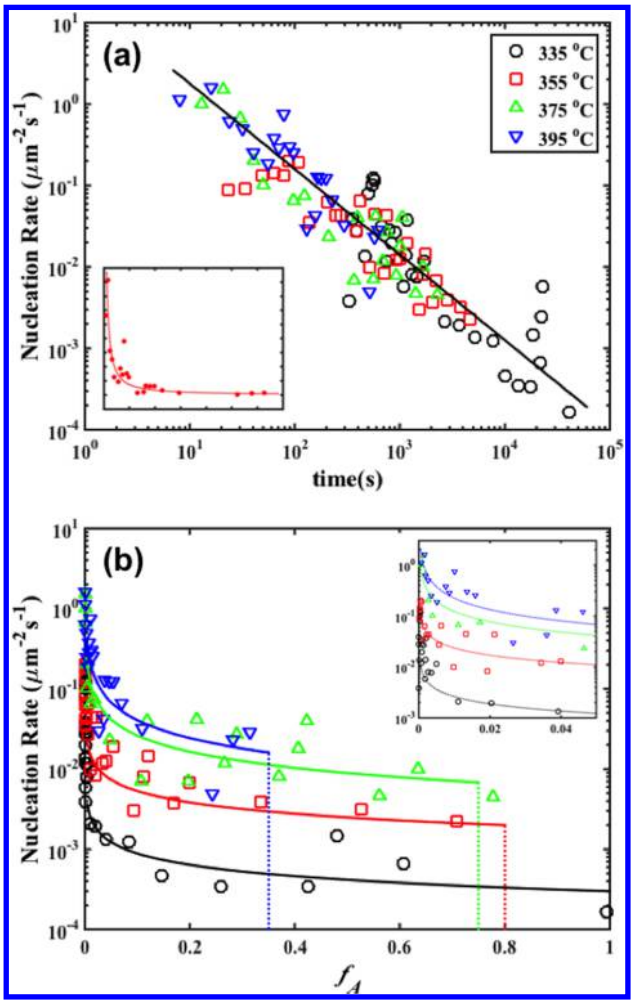

Figure 4. Nucleation mechanism. (a) Nucleation rate vs time at different temperatures. The inset shows power law decay of the nucleation rate on a linear scale. (b) Nucleation rate vs area fraction at different temperatures. The inset is an enlargement of $0 \leq f_A \leq 0.05$. The legend for panel a applies to panel b as well.

other being the surface energy.[30] The fact that the nucleation rate in this system shows power law decay indicates that either N_0 decays by a power law or W is changing logarithmically. In other words, the structural relaxation in a-ZITO-30 changes the magnitude of W over the course of crystallization. Logarithmic structural relaxation has been previously reported for various glass systems including amorphous indium oxide,[32−34] which makes the latter argument the most probable.

Figure 4b shows the nucleation rate vs crystallized area fraction. At 335 °C, which is close to the crystallization temperature of a-ZTIO-30, the nucleation process continues until the end of the transformation. However, as depicted in Figure 4b, for temperatures above 335 °C, the nucleation process stops before crystallization is finished. This phenomenon could be the result of defect annihilation at higher temperature, which leads to a sudden drop in heterogeneous nucleation sites. Obviously, increasing the temperature speeds the relaxation kinetics and accelerates the defect annihilation, which eventually results in the complete halting of nucleation, as shown in Figure 4b.

Altogether, the mixed character of the nucleation process described above certainly distinguishes a-ZTIO-30 nucleation from a classical nucleation process and makes it more attractive for further studies. More importantly, due to the non-steady-state nucleation behavior of a-ZTIO-30, employing classical JMAK analysis for this system would lead to an inaccurate picture of the crystallization process.

Growth Rate. First-order phase transformations, including crystallization from the amorphous state, take place via a nucleation and growth process. Therefore, to conduct a comprehensive kinetics study of a-ZTIO-30 crystallization, it is crucial to investigate the growth rate and growth behavior during the transformation. To determine the overall growth rate, the area evolution of at least five individual grains at a given temperature was monitored over time, and the average grain size ($\sqrt{A}$) was plotted against time, as shown in Figure 5a. This shows that the crystals are growing by interface-limited

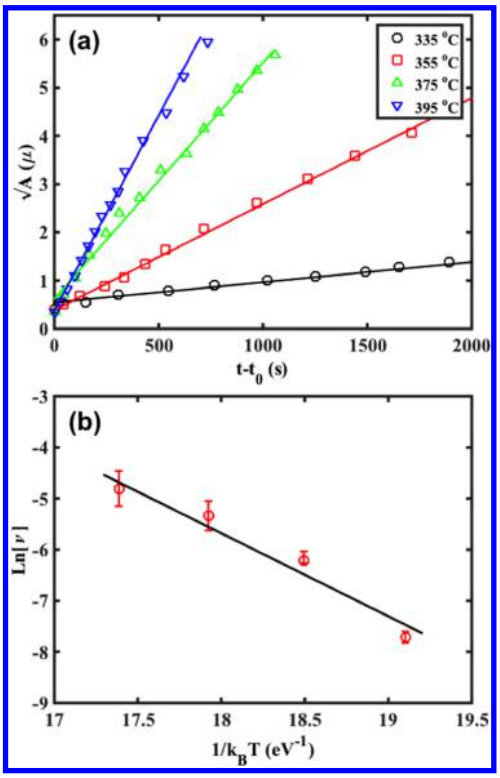

Figure 5. Interface growth. (a) Grain size vs time at different temperatures. The slope indicates the growth rate. (b) Arrhenius plot for the temperature dependence of interface growth.

kinetics since the average size of the crystals ($\sqrt{A}$) increases linearly with time. The slope of the plot is related to the overall growth rate regardless of the particle shape factor.

Figure 5a shows the change in the slope with temperature. To be more specific, the overall growth rates at 355, 375, and 395 °C are about 5, 12, and 20 times greater than that at 335 °C, respectively. Figure 5b is an Arrhenius plot for the growth rate, from which the activation energy associated with interface growth (E_G) is extracted. From the slope of the best linear fit to the measured data points, the interface growth activation energy is determined to be E_G = 1.68 eV.

The EDX spectra shown in Figure 6 confirm that there is no significant difference in the elemental distributions of the amorphous and crystalline phases. The absence of elemental segregation (a characteristic of diffusion-limited growth) also indicates that the kinetics of a-ZITO-30 crystallization is interface-limited growth. This allows a geometric model of

DOI: 10.1021/acs.cgd.6b01849
Cryst. Growth Des. XXXX, XXX, XXX−XXX

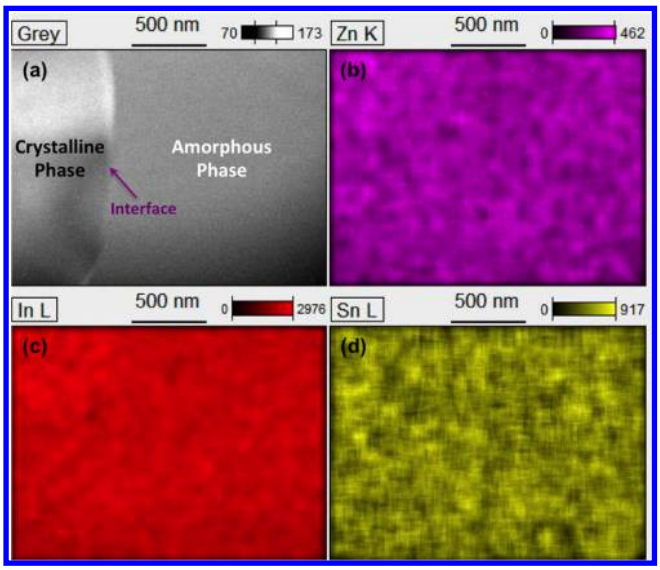

Figure 6. Elemental analysis of ZITO-30 crystallization via EDS. (a) Crystalline/amorphous interface. (b) Elemental distribution map for zinc. (c) Elemental distribution map for indium. (d) Elemental distribution map for tin. The homogeneous elemental distribution at the interface between the amorphous and crystalline phases indicates the absence of diffusion-limited growth in the system.

interface motion[35] to be employed for analyzing the growth data. In this model, the relation between the interface velocity and its thermodynamic driving force is defined by eq 2, which describes the way that the new phase evolves during the transformation to decrease the total free energy.

$$v = M[\Omega + \mathrm{wmc}] \tag{2}$$

Here, Ω is the change in the bulk free energy associated with the formation of the new crystallized volume, wmc is the weighted mean curvature, which expresses the decrease in the specific surface free energy of the interface, and M is an interface mobility, which is a proportional factor between the interface velocity and its driving force. Further analysis of the growth rate results (Figure 5a) based on eq 2 reveals that in a-ZTIO-30 crystallization the only active driving force is the Ω term and the change in the interface curvature (wmc term) has no significant contribution to interface evolution. In other words, the interfacial velocity in a-ZTIO-30 depends on the interface mobility rather than the interfacial surface energy. This interpretation is also consistent with our observations from the in situ TEM experiments (Figure 1).

Anisotropic Growth. The faceted interfaces observed during the a-ZTIO-30 crystallization process display many characteristics of anisotropic growth. To study the anisotropic behavior of this system, all grain shapes were classified according to their morphologies. These morphologies include square, regular hexagon, and a variety of semiregular hexagons.

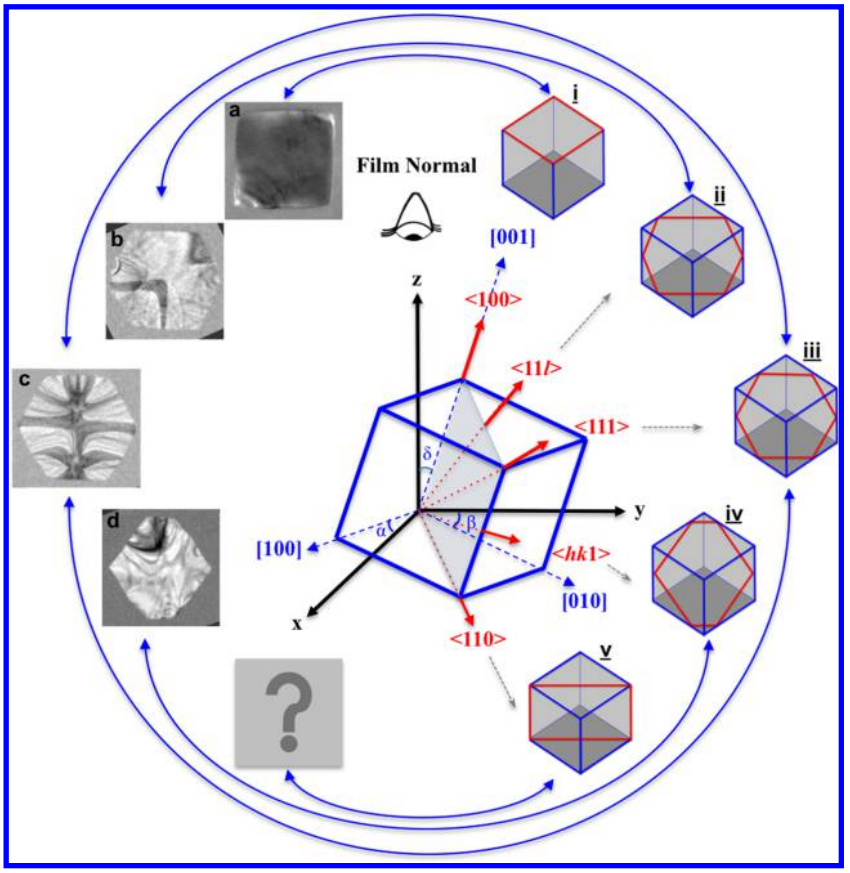

Figure 7. Morphological characterization of cube-shaped crystals: (a) square cross section under the ⟨100⟩ direction; (b) semiregular hexagonal cross section under the [11l] direction; (c) hexagonal cross sections under the ⟨111⟩ direction; (e) semiregular hexagonal cross section under the [hk1] direction (h = k). The center shows a schematic of cube-shaped crystal orientation with respect to the film normal. Red arrows demonstrate projection axes. α, β, and δ represent misorientation angles with respects to the x, y, and z axes. Inscribed red polygons in i–v depict possible growth morphologies in the cubic system while the corresponding direction axis becomes parallel to the film normal.

DOI: 10.1021/acs.cgd.6b01849
Cryst. Growth Des. XXXX, XXX, XXX−XXX

The ZITO-30 crystal structure is bixbyite, which contains 80 atoms in its unit cell[36] and has an isometric (cubic) diploidal symmetry with a lattice constant a = 10.015 Å.[37] Given the large size of this unit cell, one would expect that in this system the crystallization growth forms could be cube-shaped crystals in cubic space groups. Figure 7a–d shows the most observed morphologies at different annealing temperatures. As the highlighted cross sections in Figure 7i–iv indicate, all of these morphologies are consistent with crystal growth in a cubic system.

Cubic growth in the bixbyite crystal structure implies that ⟨100⟩ is the slowest growing direction, which consequently controls the shape of the grains. Thus, if the {100} planes of the nucleus form along the film–vapor interface, the growing crystal will have a cubic or 4-fold symmetric shape; see schematics Figure 8a and 7i. However, nonsquare shapes are

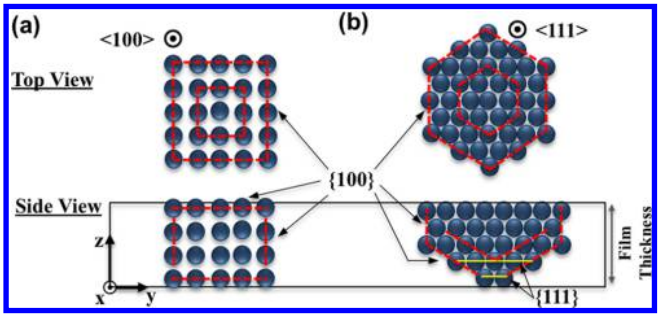

Figure 8. (a) Schematic of 4-fold symmetry in stacking layers of {100} planes intersecting {100} planes, which results in a square grain shape. (b) Schematic of 6-fold symmetry in stacking layers of {111} planes intersecting {100} planes, which results in a hexagonal grain shape. Red dashed lines illustrate the {100} planes; the yellow lines illustrate the {111} planes.

possible even if the {100} planes are the slow growth planes. If the nucleus has {111} planes that are parallel to the plane of the film–vapor interface, then a hexagonal shape is possible. This is due to the 6-fold rotational symmetry of the ⟨111⟩ axes in the cubic system; see both Figures 8b and 7iii. In the plane of the film, the growing interfaces are still {100}; see Figure 8b, where traces of the growing interface around a ⟨111⟩ direction intersect {100} planes with the same angle at every 60° of rotation (Figure 8b). Therefore, the growing crystal has six equal facets with similar interfacial mobilities, which results in a hexagonal grain shape. The same principle applies to nuclei normal to the film–vapor interface of the types ⟨11l⟩ and ⟨hk1⟩ (h = k). However, in contrast to the ⟨111⟩ axes, traces of these planes intersect surrounding {100} planes at two different angles owing to the 2-fold symmetry of the ⟨11l⟩ and ⟨hk1⟩ (h = k) axes. As a result, the interfacial mobility of the two middle facets (larger or smaller facets) differs from that of the other four, which leads to a semiregular hexagon, as shown in Figure 7ii,iv. The fact that these morphologies maintain their symmetries and shapes over time (see Supporting Information Movies S1, S2, S3, and S4) confirms that facets with different lengths grow with dissimilar but constant relative interfacial mobilities. Therefore, the observed morphologies in Figure 7b,d represent the equilibrium kinetic Wulff shapes of growing crystals in this system.

Further analysis reveals a similar growth rate for the hexagonal and square morphologies, which is another characteristic of cubic growth. Figure 7i–v illustrates how all of the inscribed cross sections within a cube grow at the same rate as the cube. Consequently, one can conclude that $1 \geq \sqrt{3}\nu_{\langle 100\rangle}/\nu_{\langle 111\rangle}$ in this system as long as there is growth with a cubic morphology.[38,39] It is also noteworthy that, among all possibilities shown in Figure 7i–v, no rectangular grain shape corresponding to the ⟨110⟩ axes is observed in this experiment (Figure 7v).

Figure 9a shows another crystal shape, which does not follow regular cubic growth. The observed cross section is consistent

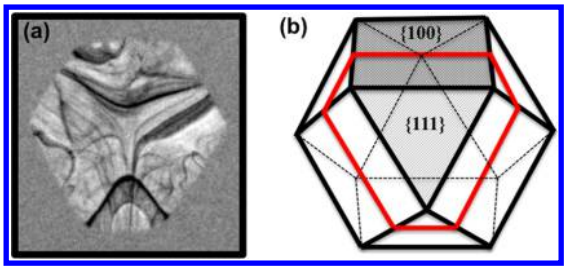

Figure 9. Semiregular hexagonal morphology observed at 335 °C. (a) Micrograph under 1000× magnification; (b) cuboctahedron structure. Red lines show the intended cross section.

with a cuboctahedron morphology and is observed only at 335 °C. As shown in Figure 9b, this particular morphology can form when nucleation starts from a {111} plane, corresponding to triangle facets in the cuboctahderon.[40–42] In this morphology, growth occurs in both the ⟨100⟩ and ⟨111⟩ directions while $1.5 \leq \sqrt{3}\nu_{\langle 100\rangle}/\nu_{\langle 100\rangle} < 2$. However, our measurements show that the lengths of the {111} planes (smaller sides) do not increase as fast as the {100} planes, which indicates that the crystal is in a transient shape and has not attained the equilibrium kinetic Wulff shape.[38,39]

The population distributions of the observed morphologies at different annealing temperatures are shown in Figure 10.

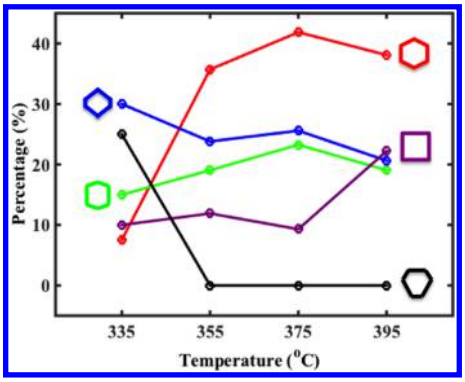

Figure 10. Population density of grain morphologies at different annealing temperatures.

Walsh and Catlow[36] showed that among all low-index planes in the indium oxide crystal structure, the family of {111} planes has the lowest surface energy due to their charge neutral termination, whereas {100} surfaces have the highest surface energy, owing to the presence of a permanent electrical dipole, and the surface energy of {110} is between that of {111} and {100}. This means that the {111} planes of a nucleus are most likely to form at the film–vapor surface. Consistent with this argument, Figure 10 shows that the total population of morphologies associated with {111} nucleation (hexagonal and cuboctahedron) is higher than the others. Furthermore, the

DOI: 10.1021/acs.cgd.6b01849
Cryst. Growth Des. XXXX, XXX, XXX–XXX

unexpected appearance of high-index nucleation planes like {$hk1$} or {$11l$} could be the result of internal bending of the {111} lattice planes,[43,44] which is quite common in ultrathin films without a supporting substrate. This phenomenon can cause deviation in the plane axis, which results in the appearance of semiregular hexagonal grain shapes (⟨$hk1$⟩ or ⟨$11l$⟩ axes). By elevating the annealing temperature, the probability of overcoming the energy barrier of {100} nuclei formation increases, which is in agreement with the observation of more square grains at higher temperature.

CONCLUSIONS

A comprehensive kinetics study of a-ZITO-30 crystallization in ultrathin films has been conducted via in situ TEM isothermal experiments to investigate nucleation and growth during the crystallization process. The results show that the nucleation rate in this system is time-dependent and continuously decelerates following a power law decay, which most probably implies logarithmic structural relaxation in a-ZITO-30. The growth rate is constant for a given temperature and does not change over time. It is also shown that interface-limited growth is the controlling mechanism of the crystallization kinetics of a-ZITO-30. A morphological study of the grains shows that the {100} planes have the lowest interfacial mobility and are responsible for the anisotropic crystal shapes. It is found that the {111} and {100} planes are the most likely to sit parallel to the film−vapor interface during the nucleation process. At all of the examined annealing temperatures, no grain with a {110} nucleation origin is observed. These results suggest considerable prospects for convergence between theory and experiments despite the complexities of crystallization dynamics in multicomponent oxide systems.

ASSOCIATED CONTENT

Supporting Information

The Supporting Information is available free of charge on the ACS Publications website at DOI: 10.1021/acs.cgd.6b01849.

Movie S1 (335 °C) (AVI)
Movie S2 (355 °C) (AVI)
Movie S3 (375 °C) (AVI)
Movie S4 (395 °C) (AVI)
Crystallization data (XLSX)

AUTHOR INFORMATION

Corresponding Author

*E-mail: v-dravid@northwestern.edu. Phone: (847) 467-1363.

ORCID

Mahyar M. Moghadam: 0000-0002-3354-9409

Author Contributions

†M.M.M. and R.L. contributed equally to this work.

Notes

The authors declare no competing financial interest.

ACKNOWLEDGMENTS

This publication is based on work supported by the Materials Research Science and Engineering Center (NSF-MRSEC) (DMR-1121262) of Northwestern University. This research made use of the EPIC and Keck-II facilities of Northwestern University's NUANCE Center, which received support from the Soft and Hybrid Nanotechnology Experimental (SHyNE) Resource (NSF NNCI-1542205), the MRSEC program (NSF DMR-1121262) at the Materials Research Center, the International Institute for Nanotechnology (IIN), the Keck Foundation, and the State of Illinois.

REFERENCES

(1) Lewis, B. G.; Paine, D. C. *MRS Bull.* **2000**, *25* (8), 22−27.
(2) Barquinha, P.; Pimentel, A.; Marques, A.; Pereira, L.; Martins, R.; Fortunato, E. *J. Non-Cryst. Solids* **2006**, *352* (9−20), 1756−1760.
(3) Fortunato, E. M. C.; Barquinha, P. M. C.; Pimentel, A. C. M. B. G.; Gonçalves, A. M. F.; Marques, A. J. S.; Pereira, L. M. N.; Martins, R. F. P. *Adv. Mater.* **2005**, *17* (5), 590−594.
(4) Ju, S.; Facchetti, A.; Xuan, Y.; Liu, J.; Ishikawa, F.; Ye, P.; Zhou, C.; Marks, T. J.; Janes, D. B. *Nat. Nanotechnol.* **2007**, *2* (6), 378−384.
(5) Grätzel, M. *Inorg. Chem.* **2005**, *44* (20), 6841−6851.
(6) Paine, D. C.; Yaglioglu, B.; Beiley, Z.; Lee, S. *Thin Solid Films* **2008**, *516* (17), 5894−5898.
(7) Kang, J.-W.; Jeong, W.-I.; Kim, J.-J.; Kim, H.-K.; Kim, D.-G.; Lee, G.-H. *Electrochem. Solid-State Lett.* **2007**, *10* (6), J75−J78.
(8) Hara, H.; Hanada, T.; Shiro, T.; Yatabe, T. *J. Vac. Sci. Technol., A* **2004**, *22* (4), 1726−1729.
(9) Uchida, T.; Kaneta, S.; Ichihara, M.; Ohtsuka, M.; Otomo, T.; Marx, D. R. *Jpn. J. Appl. Phys.* **2005**, *44* (2L), L282.
(10) Minami, T. *Thin Solid Films* **2008**, *516* (17), 5822−5828.
(11) Lippens, P.; Segers, A.; Haemers, J.; De Gryse, R. *Thin Solid Films* **1998**, *317* (1−2), 405−408.
(12) Paine, D. C.; Whitson, T.; Janiac, D.; Beresford, R.; Yang, C. O.; Lewis, B. *J. Appl. Phys.* **1999**, *85* (12), 8445−8450.
(13) Kim, M.-G.; Kanatzidis, M. G.; Facchetti, A.; Marks, T. J. *Nat. Mater.* **2011**, *10* (5), 382−388.
(14) Kwon, J.-Y.; Lee, D.-J.; Kim, K.-B. *Electron. Mater. Lett.* **2011**, *7* (1), 1−11.
(15) Harvey, S. P.; Mason, T. O.; Körber, C.; Klein, A. *Phys. Chem. Chem. Phys.* **2009**, *11* (17), 3099−3104.
(16) Moriga, T.; Edwards, D. D.; Mason, T. O.; Palmer, G. B.; Poeppelmeier, K. R.; Schindler, J. L.; Kannewurf, C. R.; Nakabayashi, I. *J. Am. Ceram. Soc.* **1998**, *81* (5), 1310−1316.
(17) Buchholz, D. B.; Proffit, D. E.; Wisser, M. D.; Mason, T. O.; Chang, R. P. H. *Prog. Nat. Sci.* **2012**, *22* (1), 1−6.
(18) Frenzel, H.; Lajn, A.; Grundmann, M. *Phys. Status Solidi RRL* **2013**, *7* (9), 605−615.
(19) González, G. B. *Materials* **2012**, *5* (5), 818−850.
(20) Proffit, D. E.; Harvey, S. P.; Klein, A.; Schafranek, R.; Emery, J. D.; Buchholz, D. B.; Chang, R. P. H.; Bedzyk, M. J.; Mason, T. O. *Thin Solid Films* **2012**, *520* (17), 5633−5639.
(21) Buchholz, D. B.; Liu, J.; Marks, T. J.; Zhang, M.; Chang, R. P. H. *ACS Appl. Mater. Interfaces* **2009**, *1* (10), 2147−2153.
(22) Yan, A.; Sun, T.; Borisenko, K. B.; Buchholz, D. B.; Chang, R. P. H.; Kirkland, A. I.; Dravid, V. P. *J. Appl. Phys.* **2012**, *112* (5), 054907.
(23) Proffit, D. E.; Philippe, T.; Emery, J. D.; Ma, Q.; Buchholz, B. D.; Voorhees, P. W.; Bedzyk, M. J.; Chang, R. P. H.; Mason, T. O. *J. Electroceram.* **2015**, *34* (2−3), 167−174.
(24) Schindelin, J.; Arganda-Carreras, I.; Frise, E.; Kaynig, V.; Longair, M.; Pietzsch, T.; Preibisch, S.; Rueden, C.; Saalfeld, S.; Schmid, B.; Tinevez, J.-Y.; White, D. J.; Hartenstein, V.; Eliceiri, K.; Tomancak, P.; Cardona, A. *Nat. Methods* **2012**, *9* (7), 676−682.
(25) Kooi, B. J.; De Hosson, J. T. M. *J. Appl. Phys.* **2004**, *95* (9), 4714−4721.
(26) Kolosov, V. Y.; Thölén, A. R. *Acta Mater.* **2000**, *48* (8), 1829−1840.
(27) Moghadam, M. M.; Voorhees, P. W. *Scr. Mater.* **2016**, *124*, 164−168.
(28) Moghadam, M. M.; Pang, E. L.; Philippe, T.; Voorhees, P. W. *Thin Solid Films* **2016**, *612*, 437−444.
(29) Edelman, F.; Weil, R.; Werner, P.; Reiche, M.; Beyer, W. *phys. stat. sol. (a)* **1995**, *150* (1), 407−425.
(30) Kelton, K.; Greer, A. *Nucleation in Condensed Matter*, 1st ed.; Pergamon, 2010. http://store.elsevier.com/Nucleation-in-Condensed-Matter/Ken-Kelton/isbn-9780080421476/.

DOI: 10.1021/acs.cgd.6b01849
Cryst. Growth Des. XXXX, XXX, XXX−XXX

(31) Lee, H.-J.; Ni, H.; Wu, D. T.; Ramirez, A. G. *Appl. Phys. Lett.* **2005**, *87* (12), 124102.
(32) Amir, A.; Oreg, Y.; Imry, Y. *Proc. Natl. Acad. Sci. U. S. A.* **2012**, *109* (6), 1850−1855.
(33) Ovadyahu, Z. *Phys. Rev. B: Condens. Matter Mater. Phys.* **2006**, *73* (21), 214204.
(34) Ovadyahu, Z.; Pollak, M. *Phys. Rev. B: Condens. Matter Mater. Phys.* **2003**, *68* (18), 184204.
(35) Taylor, J. E.; Cahn, J. W.; Handwerker, C. A. *Acta Metall. Mater.* **1992**, *40* (7), 1443−1474.
(36) Walsh, A.; Catlow, C. R. A. *J. Mater. Chem.* **2010**, *20* (46), 10438−10444.
(37) Hoel, C. A.; Gaillard, J.-F.; Poeppelmeier, K. R. *J. Solid State Chem.* **2010**, *183* (4), 761−768.
(38) Wild, C.; Koidl, P.; Müller-Sebert, W.; Walcher, H.; Kohl, R.; Herres, N.; Locher, R.; Samlenski, R.; Brenn, R. *Diamond Relat. Mater.* **1993**, *2* (2), 158−168.
(39) Smereka, P.; Li, X.; Russo, G.; Srolovitz, D. J. *Acta Mater.* **2005**, *53* (4), 1191−1204.
(40) Tao, A. R.; Habas, S.; Yang, P. *Small* **2008**, *4* (3), 310−325.
(41) Wang, Z. L. *J. Phys. Chem. B* **2000**, *104* (6), 1153−1175.
(42) Meng, M.; Wu, X.; Zhu, X.; Yang, L.; Gan, Z.; Zhu, X.; Liu, L.; Chu, P. K. *J. Phys. Chem. Lett.* **2014**, *5* (24), 4298−4304.
(43) Rimini, E.; De Bastiani, R. D.; Carria, E.; Grimaldi, M. G.; Nicotra, G.; Bongiorno, C.; Spinella, C. *J. Appl. Phys.* **2009**, *105* (12), 123502.
(44) Alberti, A.; Bongiorno, C.; Cafra, B.; Mannino, G.; Rimini, E.; Metzger, T.; Mocuta, C.; Kammler, T.; Feudel, T. *Acta Crystallogr., Sect. B: Struct. Sci.* **2005**, *61* (5), 486−491.

DOI: 10.1021/acs.cgd.6b01849
Cryst. Growth Des. XXXX, XXX, XXX−XXX